UNIVERSITY OF LEEDS

This is a repository copy of *Assessing the influence of calcium on X65 carbon steel pitting using an artificial pit*.

White Rose Research Online URL for this paper:
https://eprints.whiterose.ac.uk/213694/

Version: Accepted Version

Article:

Mohammed, S.A., Hua, Y. and Barker, R. orcid.org/0000-0002-5106-6929 (2023) Assessing the influence of calcium on X65 carbon steel pitting using an artificial pit. Materials and Corrosion, 74 (4). pp. 520-534. ISSN 0947-5117

https://doi.org/10.1002/maco.202213413

© 2022 Wiley-VCH GmbH. This is the peer reviewed version of the following article: S. A. Mohammed, Y. Hua, R. Barker, Mater. Corros. 2023; 74: 520–534, which has been published in final form at https://doi.org/10.1002/maco.202213413. This article may be used for non-commercial purposes in accordance with Wiley Terms and Conditions for Use of Self-Archived Versions. This article may not be enhanced, enriched or otherwise transformed into a derivative work, without express permission from Wiley or by statutory rights under applicable legislation. Copyright notices must not be removed, obscured or modified. The article must be linked to Wiley's version of record on Wiley Online Library and any embedding, framing or otherwise making available the article or pages thereof by third parties from platforms, services and websites other than Wiley Online Library must be prohibited.

Reuse

Items deposited in White Rose Research Online are protected by copyright, with all rights reserved unless indicated otherwise. They may be downloaded and/or printed for private study, or other acts as permitted by national copyright laws. The publisher or other rights holders may allow further reproduction and re-use of the full text version. This is indicated by the licence information on the White Rose Research Online record for the item.

Takedown

If you consider content in White Rose Research Online to be in breach of UK law, please notify us by emailing eprints@whiterose.ac.uk including the URL of the record and the reason for the withdrawal request.

White Rose
university consortium
Universities of Leeds, Sheffield & York

eprints@whiterose.ac.uk
https://eprints.whiterose.ac.uk/

Assessing the influence of calcium on X65 carbon steel pitting using an artificial pit

Sikiru Adepoju Mohammed
Defence Industries Corporation of Nigeria
&
Nigerian Defence Academy
Kaduna Nigeria

Richard Barker
Department of Mechanical Engineering
University of Leeds
Leeds, LS2 9JT
United Kingdom

Yong Hua
Department of Mechanical Engineering
University of Leeds
Leeds, LS2 9JT
United Kingdom

Anne Neville
Department of Mechanical Engineering
University of Leeds
Leeds, LS2 9JT
United Kingdom

ABSTRACT

Corrosion products that form on carbon steel in sweet (CO_2) environments can protect the steel by retarding interactions between the substrate steel and a corrosive electrolyte. Such protective films could become damaged at local sites leading to potential differences and the emergence of galvanic current with the consequence of pitting in certain environments. The large protected surface (with a higher positive potential) becomes a cathode while the tiny exposed surface (with lower positive potential) becomes the anode. Films formed in a Ca^{2+} - rich environment often comprise mixed calcium and iron carbonates in the form, $Ca_xFe_{(1-x)}CO_3$. This work utilised an artificial pit to investigate pitting under $Ca_xFe_{(1-x)}CO_3$ film conditions. Mixed carbonate films were grown on cathode discs (25mm diameter) for 96 h at pH 7.5, 50°C. Freshly polished anode pins were screwed onto the cathode disc and the galvanic currents were measured for 24 h. The anode/cathode area ratios were varied by using pins of 1mm, 2mm and 3mm diameter. SEM, XRD and EDX were employed to examine the electrode surfaces after the test while surface profilometry was conducted to obtain pit profiles on the anode pins. Galvanic current increased with the addition of 682 ppm Ca^{2+} to the solution while pseudo-passivation occurred under mixed calcium-iron carbonate films. The galvanic current was observed to drop as corrosion products formed on the anode electrode. Profilometry revealed the emergence of pits on the anode electrode. The pitting threshold was commensurate with the magnitude of galvanic current density recorded.

Keywords: X65 carbon steel, mixed carbonate, artificial pit and profilometry

1. **Introduction**

Carbon steels remain a prime choice for oil & gas applications due their low cost, mechanical properties and availability but their susceptibility to corrosion such as pitting is yet to be fully addressed[1-3]. Pitting corrosion is generally believed to evolve from localised disruption of films formed on metal. Disruption of the protective films is also a common cause of mesa attack recorded in the upstream oil & gas[4]. The compromised site, known as the anode, possesses lower potential than the surrounding cathode with higher positive potential. Solution chemistry in the pH range of 6.6 and above are often considered in flow lines to mitigate effect of top-of-line corrosion[5].

High pH in a sweet (CO_2) medium decreases solubility (promotes precipitation/scaling) of $FeCO_3$[6]. Corrosion products formed on carbon steel can retard the corrosion rate by disrupting anodic dissolution and forming a mass transfer barrier which blocks interaction of cathodic species on the metal surface[7]. Corrosion at high pH (pH>7) yields a protective film characterised by a rise in open circuit potential and sharp drop in corrosion rate; a phenomenon termed as **pseudo-passivation**[7]. Low carbon steel corroded in saturated CO_2 solution beyond 48 h at high pH becomes pseudo- passivated recording potential increases up to about 400 mV compared to a freshly polished surface[7]. No clear explanation is available to date on pseudo-passivation. Many works however believe that formation of magnetite (Fe_3O_4) beneath $FeCO_3$ layers causes the pseudo-passive effect[7, 8]. Singer[9] is of the view that high pH of electrolyte trapped between steel substrate and formed film influence formation of Fe_3O_4[9]. Despite film protectiveness, pitting corrosion was observed to occur on passive surfaces as revealed by Pessu et al.[10] who investigated the influence of pH on localized corrosion behaviour of X65 carbon steel in CO_2-saturated brines.

There are many instances where products formed on carbon steel are not entirely $CaCO_3$ but a mixture of carbonates such as $Ca_xFe_{(1-x)}CO_3$. This is expected in storage tanks harboring Ca^{2+} rich crude and down time scenarios in enhanced hydrocarbon recovery [11-15], in which pitting persists. Effects of flow, particles or chemistry change could limit protection of passive films by exposing bare steel to corrosive medium. Han et al's. [4] work on roles of passivation and galvanic effects in localized CO_2 corrosion of mild steel reported that compromised spots in a passive layer can evoke galvanic coupling.

It is generally believed that the potential difference between the anode and cathode is responsible for pitting occurrence. Potential differences in the range up to 50 mV have been utilised in several pit- ting studies conducted on low carbon steel using the artificial pit [16-18]. Having higher anode to cathode potential margin would aid accelerated pitting if such margin is actually responsible for pitting as reported in literature. Several investigations have been conducted on localised corrosion in carbon steel using an artificial pit [4, 17-20]. Most artificial pit experiments conducted were based on deposited $FeCO_3$. Knowledge is still lacking on the how the galvanic trend influences pitting under mixed carbonate conditions which is common in oil-field brines. Similarly, the artificial pit is yet to be utilised to exhaustively unravel events on compromised anode pins. This work therefore investigated the effect of Ca^{2+} on X65 carbon steel pitting by forming mixed Ca^{2+} and Fe^{2+} carbonates on cathode discs and coupled a freshly polished anode onto the disc. The galvanic trend was measured followed by comprehensive analysis of both anode and cathode electrodes. White light interferometry was conducted to assess the extent of pitting on the anode pins.

2. **Artificial pit design and test procedure**

Several artificial pit designs have been developed to investigate pitting corrosion. These include Newman's artificial pit[21] ,Turnbull's pencil pit [22, 23] and Marsh's artificial pit[24]. Other pit models developed include Jiabin et al. [18], Han et al. [17] and Amri et al.[25]artificial pit. Separation of the anodic compartment from the cathodic enabled parameters to be varied in separate compartments as featured in Turnbull's model but Ohmic drop registered during measurement was a setback to this approach. For pitting investigation, it is desirable for the anode and cathode to be isolated but as close as possible in the same solution. Localised corrosion often propagates when galvanic coupling exists between large protected cathode in close proximity with tiny film-free anode. Amri and Han models are suitable for investigating pitting corrosion due to close proximity of electrodes and ease of incorporating both electrodes within the same cell. An improved artificial pit was designed in this work to mimic events in a Ca^{2+} rich corrosion pit. The anode pin and cathode disc are two important components of the artificial pit model featured in Figure 1. The artificial pit designed for this work was inspired by Amri et al's model [25] adopted in a methodology from Amri et al's [17] work on localised corrosion propagation in CO_2 systems.

The innovation in the pit design was the ability to vary the pit depth by turning an insulated nylon bolt whose tip was the anode electrode. The anode was made of variable pins (1mm, 2mm and 3mm diameter) embedded in a nylon bolt where the thread pitch was used to control anode displacement (pit depth). One complete turn of the nylon bolt displaces the anode by 1.25mm. Anode and cathode of the artificial pit shown in Figure 2(a) were made of X65 (UNS K03014) carbon steel. The cathode was machined from cylindrical bar to disc shape of 4.9 cm^2 (diameter of 25mm with thickness of 5mm) and masked in heat resistant resin. A 9 mm hole was drilled all through the centre of the cathode and filled with resin which bears the thread through which the nylon bolt runs. The anode pin was machined in sets of 1mm, 2mm and 3mm diameter. A 4.2 mm centre hole was drilled all though the length of a nylon bolt to accommodate the anode pin and connection cable. The anode pin with its cable was further insulated in resin sheath inside the nylon bolt. The artificial pit assembly was immersed in electrolyte contained in 1,000 ml glass beaker featured in Figure 2(b).

2.1. Cathode disc passivation

The artificial pit cathode was pre-passivated be- fore inserting a freshly polished anode for the galvanic experiment. The solution pH and temperature were set in line with the test matrix contained in Table 1. Linear Polarisation Resistance (LPR) and Open Circuit Potential (OCP) measurements were conducted for up to 4 days to produce pseudo- passive films. The anode pin was then polished using SiC in grit sequence from 120 to 1,200 and then coupled to a passivated cathode. ACM Gill AC potentiostat was utilised for measuring galvanic (mixed) potential/current density established after screwing a freshly polished anode (with relatively lower potential) onto the cathode (having higher potential). As a baseline, an initial test was conducted in Ca^{2+}- free solution to compare with experiments conducted in a Ca^{2+} solution. Tafel plots and derivatives for electrochemical measurements conducted in 682 ppm Ca^{2+} solution are shown in Figure 3 and Table 2 respectively. Preliminary tests were conducted using 3.3 wt.%, 3.1 wt.%NaCl separately in 682 ppm & 1364 ppm Ca^{2+} solutions, while maintaining 21,233 ppm chloride concentration. Chloride level was kept constant to ensure the accuracy of pitting data collected as variation in chloride concentration could alter the pitting kinetics. Although calcium content in formation water can exceed 5,000 ppm, experiments in this section were conducted using 682 ppm Ca^{2+} as higher Ca^{2+} concentrations diminish the magnitude of galvanic current needed to conduct artificial pit investigations. The trend observed under this condition can be inferred in solutions containing higher Ca^{2+} concentration. A pH of 7.5 was used to ensure faster precipitation of mixed $Ca_xFe_{(1-x)}CO_3$ films at 50 ºC.

Table 1: Artificial pit test matrix

Item	Description	Value
Metal specification	X65 Cathode diameter Anode diameter Anode/cathode ratio	0.07 to 0.12%C 25mm 1mm, 2mm and 3mm 1:625, 1:156 and 1:69
Film growth on cathode	Duration pH Temperature Magnetic stirrer	96 h pH7.5 50°C 100 rpm
Test cell condition	Duration De-ionised water pH Temperature Pit depth Magnetic stirrer Brine* Brine**	24Hrs 1,000ml pH7.5 50 °C 0.625mm Near-static 3.5 wt% NaCl, pH7.5 3.3 wt% NaCl, pH7.5 0.25 wt%$CaCl_2.2H_20$

*21,233ppm Cl^- & 0 ppm Ca^{2+}

**21,233ppm Cl^- & 682 ppm Ca^{2+}

Table 2: Tafel Constant

pH	Temp (°C)	β_a(mV/decade)	β_c(mV/decade)	B(mV/decade)	I_{corr}(mA/cm^2)
* pH 7.5	50 °C	100	80	19.30	0.15

3. Results/Discussion

Top-view SEM and LPR/OCP plots of initial tests are shown in Figure 4 and Figure 5 respectively. Only $FeCO3$ crystals of different sizes form in Ca^{2+}- free solution as expected and are shown in Figure 4(a). Mixed carbonate crystals ($Ca_xFe_{(1-x)}CO_3$) were formed in 682 ppm Ca^{2+} - solution (Figure 4(b)). The crystal size however became smaller as calcium concentration was increased to 1,264 ppm as shown in Figure 4(c). The film formed on the passivated cathode plays a significant role in determining the galvanic trend of the artificial pit. Detailed SEM images of the film formed after corrosion tests in 682 ppm Ca^{2+} solution for 96 h are shown as Figure 8. Crystals with attributes similar to both Calcite and Siderite ($FeCO_3$) crystals were recorded. This is in contrast to crystals observed for films in Ca^{2+} - free systems where smaller crystals fuse within cavities of larger crystals (Figure 4(a). A look at the LPR results featured in Figure 5 shows that tests conducted in 3.3 wt% NaCl, 682 ppm Ca^{2+} (depicted in red) offered the lowest corrosion rate and there- fore were considered appropriate for the artificial pit experiment since the highest galvanic currents were expected in the event of film break down.

A pseudo-passive trend was observed on the steel surface after about 48 h in Ca^{2+} - free solution (Figure 6) while pseudo-passivation trend was delayed for solutions containing 682 ppm Ca^{2+} as shown in Figure 7. Several inconclusive theories relate to pseudo-passivity[7, 8] and around this phenomenon. For Ca^{2+} - free systems, the corrosion rate was observed to drop from about 1.5 mmpy to 0.15 mmpy after 24 h. OCP however increases spontaneously by 400 mV after 48 h. For solutions containing 682 ppm Ca^{2+}, a pseudo-passive trend was less rapid and became pronounced after about 72 h exposure. A delay in pseudo-passivation with 682 ppm Ca^{2+} suggests that the Ca^{2+} ions retard the film building process.

3.1 *Analysis of mixed carbonate formed in 682 ppm Ca^{2+}*

Figure 8 shows different magnification SEM images of the products formed on artificial pit cathodes before the anode pin was coupled. The images depict a mixture of crystals whose EDX elemental scan (Figure 9) suggests $Ca_xFe_{(1-x)}CO_3$ hexagonal crystals. $Ca^{2+}$and Fe^{2+} were detected in net percentages of 3.05 and 19.61 respectively. This implies that molar fractions of Ca^{2+} to Fe^{2+} in the $Ca_xFe_{(1-x)}CO_3$ mixture were 0.13 to 0.87 respectively. Detailed XRD analysis was conducted to corroborate the EDX scan results. An XRD scan of the crystals formed on X65 carbon steel corroded in 682 ppm Ca^{2+} for 4 days before coupling the anode for galvanic measurement is shown in Figure 10. XRD analysis using the high- *score* software revealed the presence of a hexagonal crystal lattice whose properties lie between calcite and $FeCO_3$. Matching experimental XRD peaks with literature results aligned in Figure 10 shows that peak detected at 31.7999 °2Theta fell between $CaCO_3$ and $FeCO_3$ but much closer towards the latter. This suggests a higher proportion of Fe^{2+} in the mixed carbonate structure which is in agreement with the molar fraction revealed in the EDX result featured in Figure 9. Detailed composition of Ca^{2+} and Fe^{2+} was further investigated using cell parameters of XRD peaks detected at 31.7999 °2Theta.

A typical hexagonal diagram of $CaCO_3$ and $FeCO_3$ crystal is featured as Figure 11. Values of a and c were calculated using the d spacing equation for a hexagonal system featured in Equation 1 [26, 27] while unit cell volume, v, was obtained using Equation 2, derived from Bragg's law [26, 27].

The Bravais lattice planes, expressed in terms of Miller indices h, k, l were obtained from X-Ray scanned data. From XRD data obtained, $h = 1$, $k = 0$, $l = 4$ for peak at 31.7999 °2Theta position. The terms "a" and "c" are unit cell edges, obtainable by substituting for known parameters in Equations 1 and 2 [28]. The d-spacing, (d_{hkl}) was also obtained from XRD scan data. d_{hkl} = 2.817 45Å for crystal peak detected at 31.7999 °2Theta position.

$$\frac{1}{d^2_{hkl^2}} = \frac{4}{3}\left(\frac{h^2+hk+k^2}{a^2}\right) + \frac{l^2}{c^2} \qquad 1$$

$$v = \frac{\sqrt{3}}{2}a^2c \qquad 2$$

Davidson et al. [29] provided data which relates cell parameters *c* and *v* of the hexagonal crystal structure with the molar fraction of constituting cations. Application of Davidson's data was demonstrated in a work by Esmaeely et al. [28] who investigated how the presence of calcium influences carbonate film protectiveness. Figures 12 and 13 were plotted from *c* and *v* parameters provided by Davidson et al.[29]. The slope of regression lines obtained from points plotted from Davidson's data correspond to molar fraction, x in $Ca_xFe_{(1-x)}CO_3$ [28, 29]. Equations 3 and 4 derived from Figures 12 and 13 respectively, therefore provides an expression for presenting crystal parameters as a function of molar fraction, *x*.

$$\text{Lattice parameter, } c = 1.63x + 15.39 \qquad 3$$

$$\text{Unit cell volume, } v = 74.88x + 289.47 \qquad 4$$

Where "x" is the molar fraction of Ca in $Ca_xFe_{(1-x)}CO_3$.

The value of *x* can be derived by substituting equations 2, 3 and 4 into equation 1. The *x* value derived by solving Equation 1 for peak detected at 31.7999 °2Theta was 0.13. This implies that the crystal comprised of 0.13 and 0.87 molar fraction of $Ca^{2+}$and Fe^{2+}respectively. The result matches perfectly with molar ratio revealed from EDX investigation and it is in reasonable agreement with the position of the XRD peak detected at 31.7999 °2Theta (Figure 10). This confirms that molar ratio of $Ca^{2+}$and Fe^{2+} in formed $Ca_xFe_{(1-x)}CO_3$ film was 0.13 and 0.87 respectively.

3.2 Pitting trend in 682 ppm Ca^{2+}

The galvanic trend for coupled 1mm, 2mm and 3mm anodes of 0.625 mm depth in 682 ppm Ca^{2+} is shown in Figures 14, 15 and 16 respectively. Galvanic current was high at the start of experiments but rapidly declined during the first hour of exposure due to the high initial corrosion rate of the anode which was rapidly passivated. The current drops primarily due to the disruption in potential balance as the system got settled. Since measured galvanic current density is positive, the freshly polished pin (having less positive potential) is the anode in the pit coupling[20]. Spikes emerging from galvanic trend are likely attributed to pitting on the anode pin as the spikes trended in the positive direction. The potential of the large passivated cathode disc was about -400 mV (vs Ag/AgCl) while for the freshly polished anode pin it was about -750 mV (vs Ag/AgCl) in same solution when un-coupled. Upon coupling, the mixed potential recorded was very close to that of the uncoupled cathode (-400 mV (vs Ag/AgCl)), due to the larger size of the cathode. As the anode pin corrodes in the coupling, its potential increases in the positive direction, but this event is masked by the overriding potential of the already passivated cathode disc.

The galvanic current generated by the coupling drops slowly as the potential of the anode increased. Relating figures 14, 15 and 16 to galvanic current recorded in Ca^{2+} - free solution (Figure 17) indicated higher current density for solution containing 682 ppm Ca^{2+}. While average current density of 0.25

mA/cm^2, 0.12 mA/cm^2 and 0.02 mA/cm^2 were respectively recorded for 1mm, 2mm and 3mm pits in 682 ppm Ca^{2+} solution, average current densities of 0.1 mA/cm^2, 0.05 mA/cm^2, and 0.009 mA/cm^2 were recorded for 1mm, 2mm and 3mm anodes in Ca^{2+} - free solution. The top ten average pit depths on 1mm, 2mm and 3mm anodes coupled in artificial pit for 24 h in 682 ppm Ca^{2+} solution were approximately 60μm, 34μm and 25μm respectively. Profilometry results of the maximum pit recorded on the anode electrodes after 24 h pit coupling in 682 ppm Ca^{2+} solution are featured in Figure 18. Connecting these with the galvanic trend (Figures 14, 15 and 16) suggests that pit depth increases with a rise in galvanic current as expected. Though temperature was kept constant at 50°C in this work, the pitting trend tallies with work by Han et al.[19] who reported an increase in localised attack with rise in temperature and cathode to anode area ratio (AR). AR of anode to cathode was observed to influence the magnitude of galvanic current. Average current density for 1 mm anode (AR 1:625), 2 mm anode (AR 1:156) and 3 mm anode (AR 1:69) in 682 ppm Ca^{2+}solution was 0.25 mA/cm^2, 0.12 mA/cm^2 and 0.019 mA/cm^2 respectively. This is in agreement with findings in other galvanic experiments[17, 19, 20]. For experiments conducted in Ca^{2+}- free solution, the maximum pit depths on the 1mm, 2mm and 3mm anode coupled pits for 24 h were 37μm, 22μm and 20μm respectively. A bar chart comparing pitting on anodes of coupled pits in 682 ppm Ca^{2+} and Ca^{2+} - free systems is shown in Figure 23. Higher galvanic current and pitting was recorded under mixed ($Ca_xFe_{(1-x)}CO_3$) film conditions.

SEM analysis of anode surface after 24 h pit coupling revealed presence of mixed $Ca_xFe_{(1-x)}CO_3$ deposited on the anode as shown in Figure 21. This implies that pits initiate and propagate beneath he formed film. Presence of multiple pits on anode pins (Figure 19) also suggest that micro-pitting develops within pits and that several anode/cathode spots spatially evolve on actively corroding pit sites. Presence of Ca^{2+} on anode could be responsible for the significant galvanic current and pitting recorded in artificial pit containing 682 ppm Ca^{2+}.

3.3 Measured corrosion rate for anode and cathode electrodes

Approximate corrosion rate of uncoupled cathode and anode electrodes were obtained by briefly interrupting galvanic measurement for 1mm pit in order to take LPR/OCP measurement after about 1 h, 12 h and close to end of 24 h galvanic test. The mixed (galvanic) current density after 1 h, 12 h and 24 h in coupled pit was 1.3 mA/cm^2, 0.22 mA/$cm^2$and 0.15 mA/cm^2 respectively. The galvanic current was obtained by multiplying the surface area of the anode electrode with the galvanic current density in order to derive corrosion rate for coupled anode and cathode. Corrosion rate for coupled anode and coupled cathode was calculated by factoring electrode surface area into Equation 5[30].

$$\boldsymbol{Corrosion\ Rate\ (mmpy) = 3.27 \text{ x } 10^{-3}\frac{I \text{ x } E_w}{A\ell}} \qquad 5$$

Where:
3.27 x 10-3 = constant for expression in mmpy,
I = corrosion current in μA, (derived as galvanic current in Table 3),
A= Area of electrode in cm^2, $\boldsymbol{\ell}$ = metal density in (g/cm^3), 27.5 g/cm^3 for Fe.
E_w = equivalent weight (27.56g)

A summary of applied data is presented in Table 3 while Figure 20 illustrates the corrosion rates for uncoupled and coupled pit electrodes. Corrosion rate of electrodes generally reduce as exposure time increases. The corrosion rate of the coupled anode (Figure 20) was high at the start of the experiment but declined steadily with time. This was due to fast deposition of corrosion product on the pit anode as observed in Figure 21. EDX examination of pit anode shows presence of mixed carbonate in the pit. Similar results were obtained on the anode electrode for tests conducted in Ca^{2+} - free solution where $FeCO_3$ was detected in the pit (Figure 22). It implies that similar product formed on steel surface also forms within corrosion pit. Pitting observed on anode electrode in Ca^{2+} - free coupling were of low magnitude. A bar chart depicting the top-10 average pits for Ca^{2+} - free and 682 ppm Ca^{2+} solutions is featured in Figure 23. A lower corrosion rate was also reported for the anode electrode in the work by Han et al. [17] who investigated galvanic trend in CO_2 corrosion using the artificial pit. Higher corrosion rates observed on coupled anode electrodes was due to the influence of Ca^{2+} on the mixed carbonate formed on the pit anode.

Table 3: Corrosion data obtained using 1mm anode pit coupling

Elapsed coupling time	1 h	12 h	24 h
Galvanic Current	1.3 mA/cm^2	0.22 mA/cm^2	0.15 mA/cm^2
Galvanic Current	0.010 mA	0.0017 mA	0.0012 mA
Uncoupled anode	1.2 mmpy	0.9 mmpy	0.20 mmpy
Uncoupled cathode	0.06 mmpy	0.06 mmpy	0.05 mmpy
Coupled anode	14.59 mmpy	2.48 mmpy	1.75 mmpy
Coupled cathode	0.023 mmpy	0.0039 mmpy	0.0028 mmpy

3.4 Derivation of charge associated with galvanic current in artificial pit

Figure 23 features a comparison of pitting recorded under a galvanic influence in the artificial pit. The corresponding charge was derived from the galvanic current density measured during 24 h coupling in a 682 ppm Ca^{2+} and Ca^{2+}- free solutions by integrating the product of measured current (*I*) with time (t) as presented in Equation 6. Electrochemical measurements were taken at intervals of 60 seconds covering 24 h galvanic test duration.

$$\mathbf{Q = \int_0^{24h} \boldsymbol{I\,dt} = \int_0^{24h} \boldsymbol{i\,Ad\,t}} \qquad \mathbf{6}$$

Where Q is the total charge recorded after 24 h galvanic test measured at intervals of 60 seconds, 'i' is current density (A/m^2) and 'A' is test surface area (m^2). To relate the total charge derived to the pit anode size, charge density was calculated by dividing the total charge by the area of the anode electrode. Table 4 shows the charge density with respect to the anode electrodes in Ca^{2+} - free and 682 ppm Ca^{2+} solution. A plot depicting charge density in coupled artificial pit for 682 ppm Ca^{2+} and Ca^{2+}-free solutions is shown as Figure 24. Charge densities in 682 ppm Ca^{2+} solutions were generally higher than that observed Ca^{2+}- free solutions. The charge per unit area also drops as the pit anode size increased. From Figure 24 and Figure 23, it is safe to state that Ca^{2+} presence increase pitting in low carbon steel. It as well shows that higher pit depth recorded in 1mm pit was due to higher charge density on the anode electrode. This implies that a tiny compromised spot on the film formed on carbon steel would produce higher charge density with greater consequence than compromised spot of larger size.

Table 4: Charge recorded in artificial pit coupling in saturated CO_2, 3.3 wt.% NaCl, pH 7.5, 50°C in 682ppm $\boldsymbol{Ca^{2+}}$ and $\boldsymbol{Ca^{2+}}$- free solutions

Anode Diameter	**0 ppm Ca^{2+}**		**682 ppm Ca^{2+}**	
	Total Charge	Charge Density	Total Charge	Charge Density
1mm	0.07 C	8.45 C/cm^2	0.18 C	23.00 C/cm^2
2mm	0.14 C	4.47 C/cm^2	0.45 C	14.49 C/cm^2
3mm	0.09 C	0.13 C/cm^2	0.12 C	1.68 C/cm^2

4 Conclusions

An investigation was conducted on the influence of Ca^{2+} on pitting corrosion in saturated CO_2 environment using an artificial pit. The following are the major findings revealed:

a. Calcium presence increases the galvanic current between film covered and compromised spots on low carbon steel.

b. Galvanic current density declines as corrosion products forms inside the pit.

c. Pseudo-passivation is delayed under $Ca_xFe_{(1-x)}CO_3$ film condition compared to that observed in $FeCO_3$ film.

d. Corrosion products that form on steel surface also grow within pits while micro-level stochastic pits emerge beneath the film on pit anodes.

e. The extent of pit penetration under galvanic influence depends on the area of compromised spot on the film.

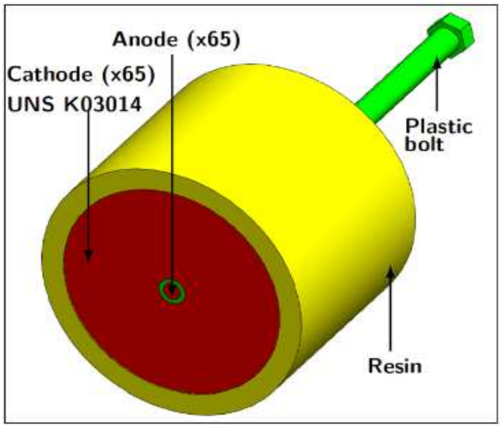

Figure 1: Artificial pit showing materials components of artificial pit

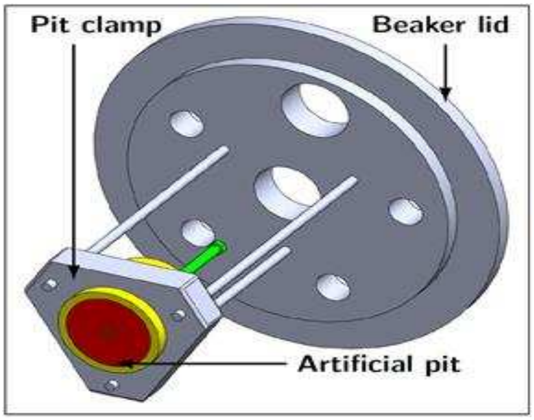

(a) Pit Assembly

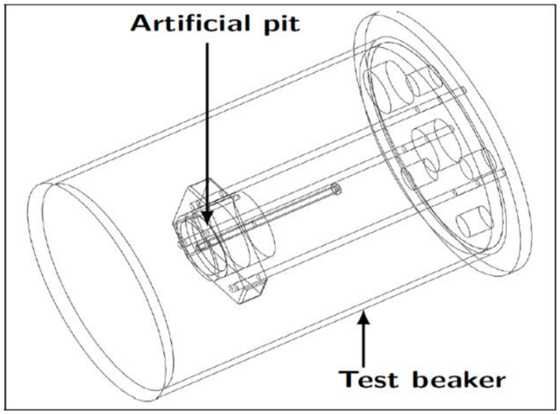

(b) Test Beaker

Figure 2: Artificial pit design for pitting corrosion test featuring (a) pit assembly and (b) pit assembly in test beaker

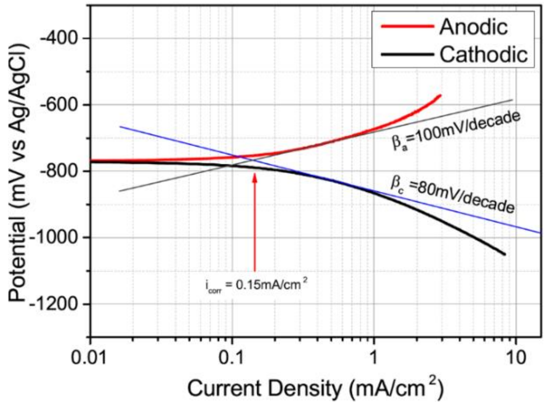

Figure 3: Tafel plots showing I_{corr}, β_a and β_c derivatives for experiment conducted in saturated CO_2, 2 wt.% NaCl, 50 °C containing 682 ppm Ca^{2+}, pH 7.5

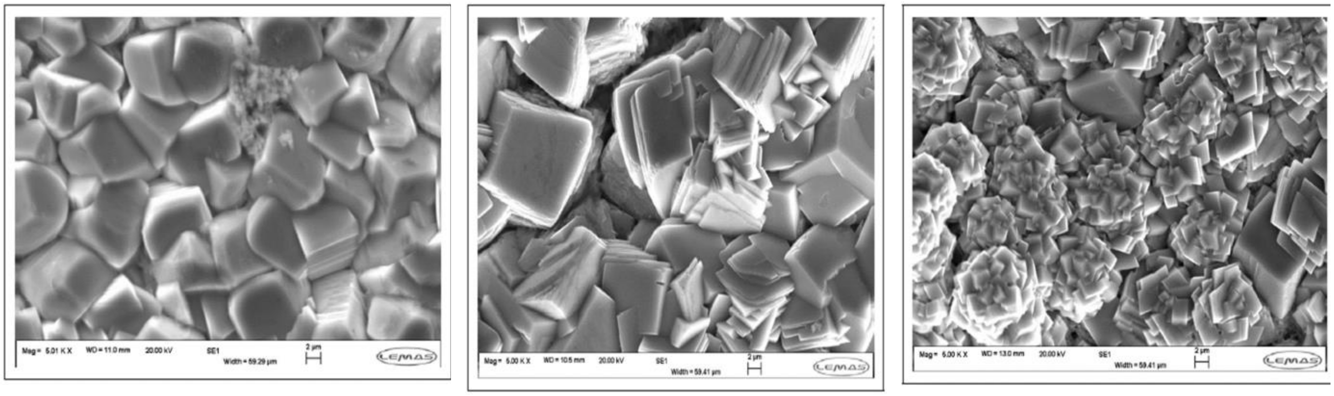

(a) 3.5wt%NaCl, 0ppm Ca^{2+} (b) 3.3wt%NaCl, 682ppm Ca^{2+} (c) 3.1wt%NaCl, 1364 ppm Ca^{2+}

Figure 4: Top-view SEM image of mixed $Ca_xFe_{(1-x)}CO_3$ formed on X65 carbon steel corroded for 96 h at pH 7.5, saturated CO_2 in (a) 3.5 wt% NaCl, 0 ppm Ca^{2+} (b) 3.3 wt% NaCl, 682 ppm Ca^{2+} and (c) 3.1 wt% NaCl, 1364 ppm Ca^{2+}

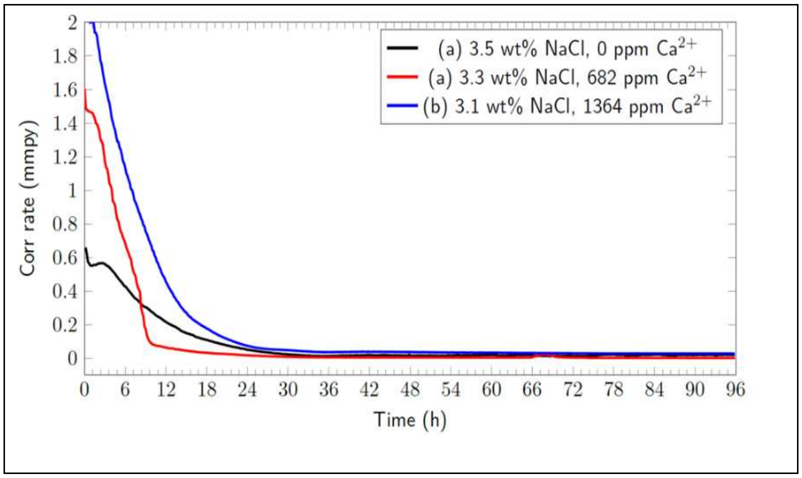

Figure 5: LPR/OCP plot for X65 carbon steel corroded for 96 h at pH 7.5, saturated CO_2 in (a) 3.5 wt% NaCl, 0 ppm Ca^{2+} (b) 3.3 wt% NaCl, 682 ppm Ca^{2+}, (c) 3.1 wt% NaCl, 1364 ppm Ca^{2+}

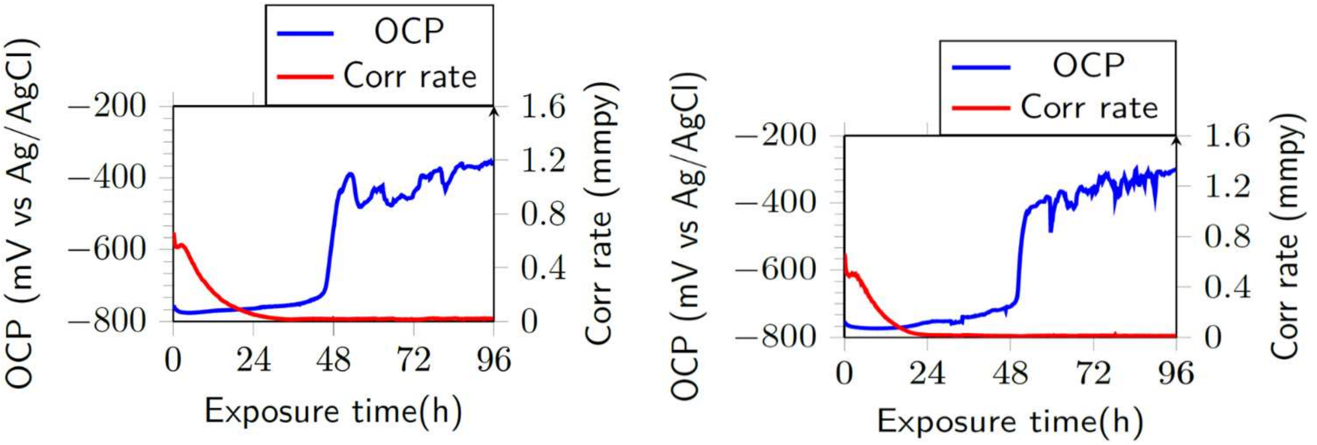

(a) Test-1 (0 ppm Ca^{2+}) (b) Test-2 (0 ppm Ca^{2+})

Figure 6: (a) Test 1 and (b) Test 2 result for LPR/OCP plot of X65 carbon steel corroded in 21,000 ppm Cl, at 50 °C, pH 7.5 for 96 h in 0 ppm Ca^{2+}

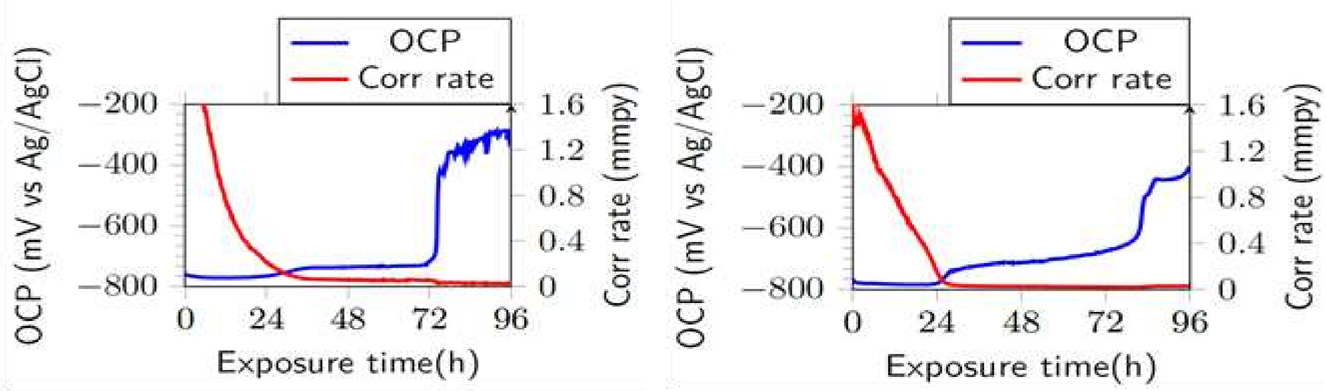

(a) Test-1 (682 ppm Ca^{2+}) (b) Test-2 (682 ppm Ca^{2+})

Figure 7: (a) Test 1 and (b) Test 2 result for LPR/OCP plot of X65 carbon steel corroded in 21,000 ppm Cl, at 50 °C, pH 7.5 for 96 h in 682 ppm Ca^{2+}

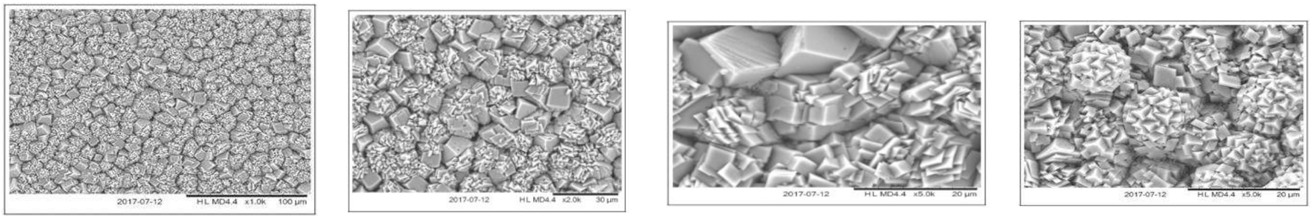

(a) (b) (c) (d)

Figure 8: Top view SEM showing mixed $FeCO_3$ and $CaCO_3$ formed on X65 carbon steel corroded in 3.3 wt% NaCl, 682 ppm Ca^{2+}, 50 °C for 96 h at pH 7.5 under (a) X1000 (b) X2000 (c) X5000 magnification and (d) calcite cluster zoom

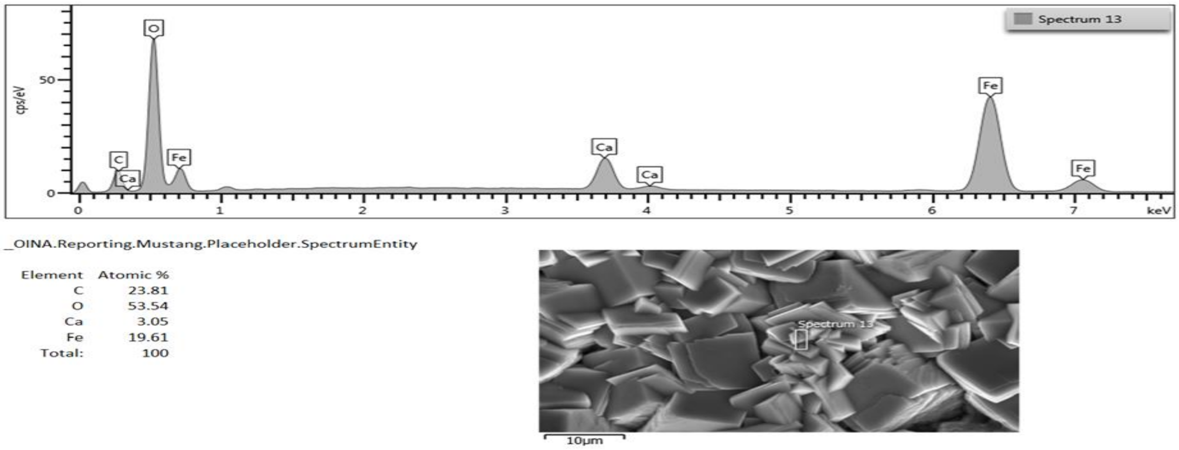

_OINA.Reporting.Mustang.Placeholder.SpectrumEntity

Element	Atomic %
C	23.81
O	53.54
Ca	3.05
Fe	19.61
Total:	100

Figure 9: EDX showing percentage composition of elements detected on X65 carbon steel corroded in 2 wt% NaCl, 682 ppm Ca^{2+}, 50 °C for 96 h at pH 7.5

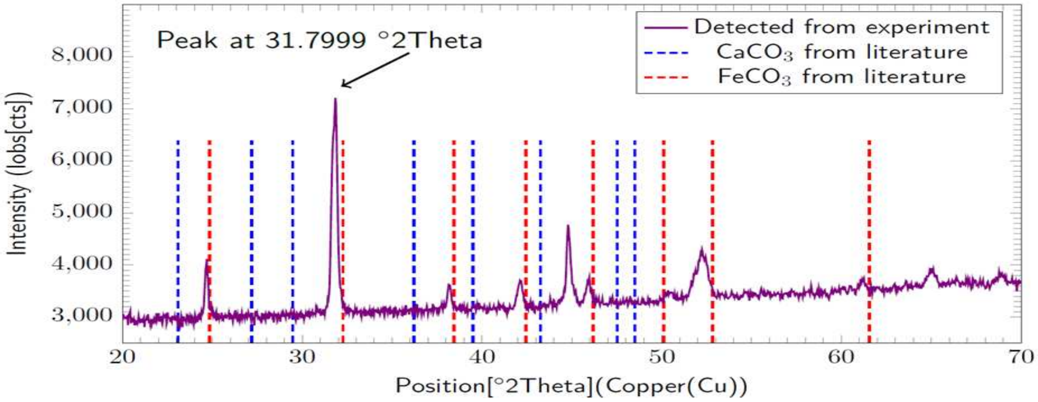

Figure 10: Plot depicting comparison of XRD °2Theta position of $CaCO_3$ and $FeCO_3$ from literature to that of detected peaks for X65 carbon steel corroded in 3.3 wt% NaCl, 682 ppm Ca^{2+}, 50 °C for 96 h at pH 7.5

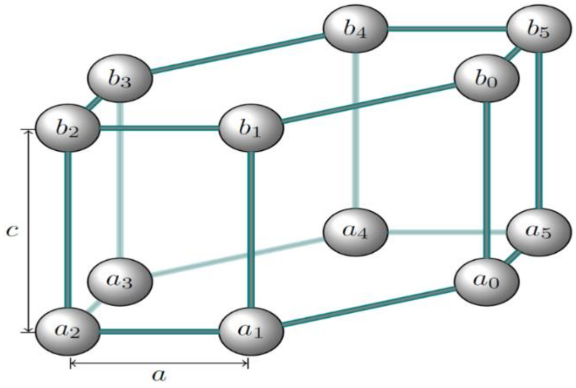

Figure 11: Schematic representation of a typical hexagonal lattice structure

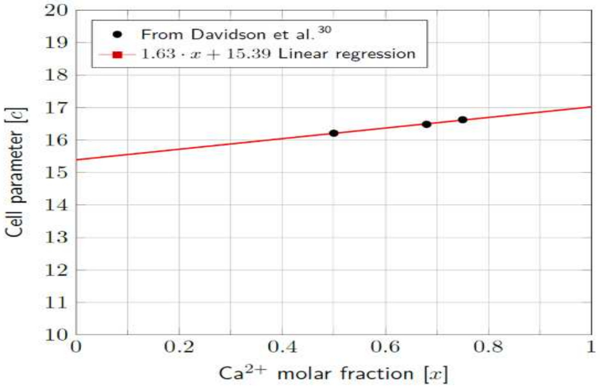

Figure 12: Plot of parameter "c" versus molar fraction of Ca^{2+}

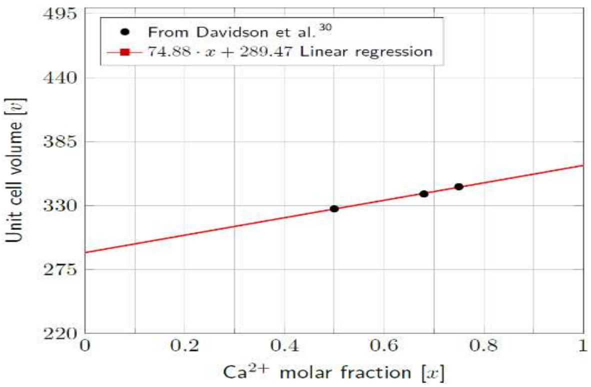

Figure 13: Plot of unit volume "v" versus molar fraction of Ca^{2+}

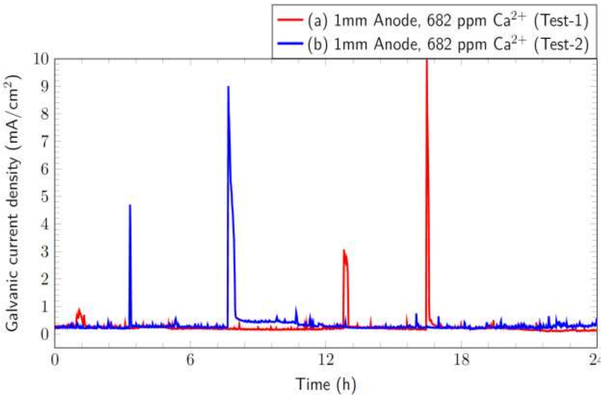

Figure 14: Repeated galvanic trend for freshly polished (a) 1mm anode (Test1) and (b) 1mm anode (Test-2) in 0.625mm pit for 24 h in 3.3 wt% NaCl, 682 ppm Ca^{2+} at 50 ◦C, pH 7.5, saturated CO_2

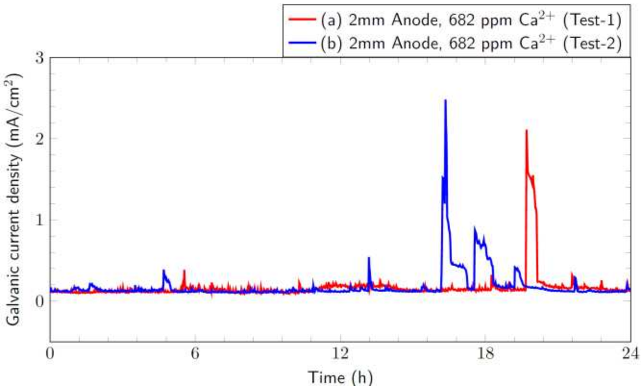

Figure 15: Repeated galvanic trend for freshly polished (a) 2mm anode (Test1) and (b) 2mm anode (Test-2) in 0.625mm pit for 24 h in 3.3 wt% NaCl, 682 ppm Ca^{2+} at 50 ◦C, pH 7.5, saturated CO_2

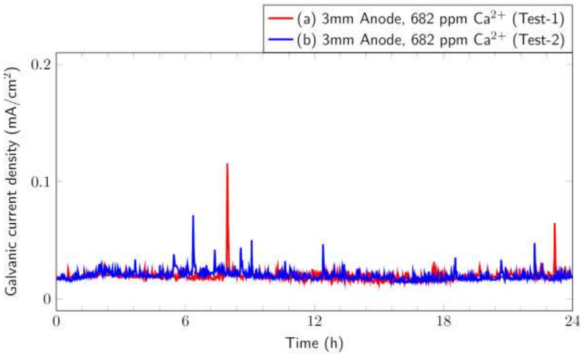

Figure 16: Repeated galvanic trend for freshly polished (a) 3mm anode (Test1) and (b) 3mm anode (Test-2) in 0.625mm pit for 24 h in 3.3 wt% NaCl, 682 ppm Ca^{2+} at 50 ◦C, pH 7.5, saturated CO_2

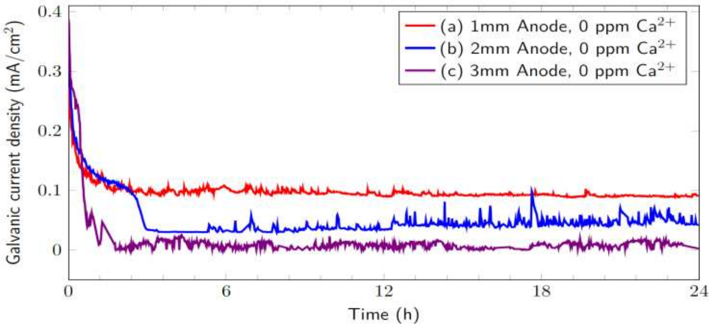

Figure 17: Galvanic trend for freshly polished (1) 1mm anode, (b) 2mm anode and (c) 3mm anode in passivated 4.9 cm^2 cathode, 0.625mm pit for 24 h in 3.5 wt% NaCl, 0 ppm Ca^{2+} at 50 ◦C, pH7.5, saturated CO_2

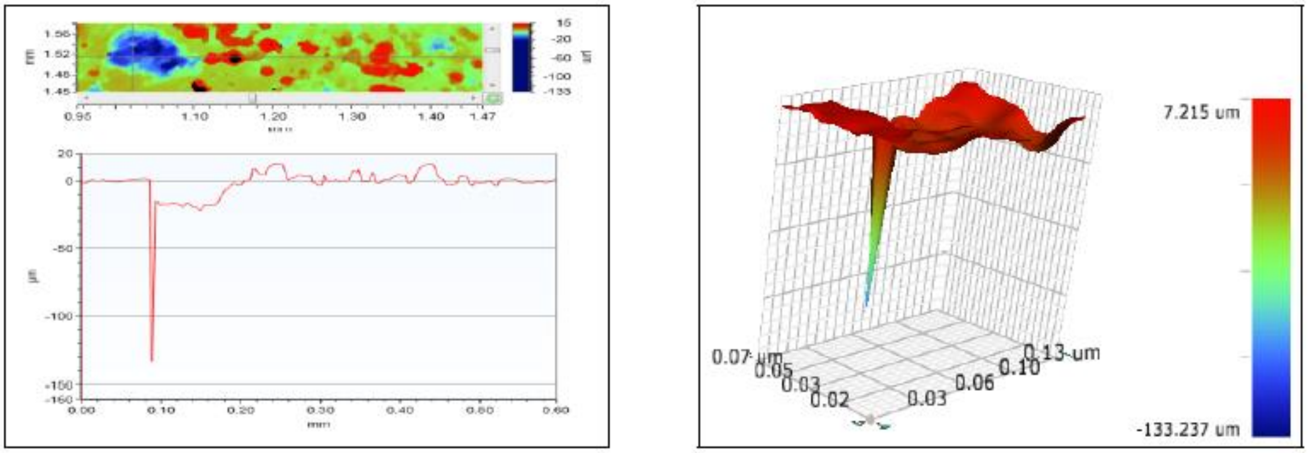

(a) **133** μ**m** pit (2D) for **1 mm Anode**

133 μ**m** pit (3D) for **1 mm Anode**

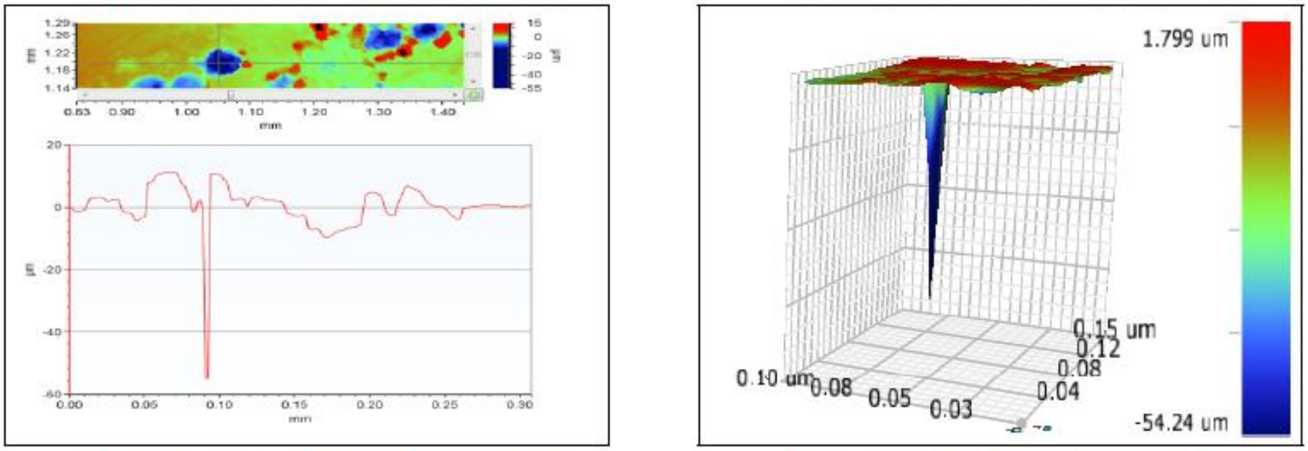

(b) **54** μ**m** pit (2D) for **2 mm Anode**

54 μ**m** pit (3D) for **2 mm Anode**

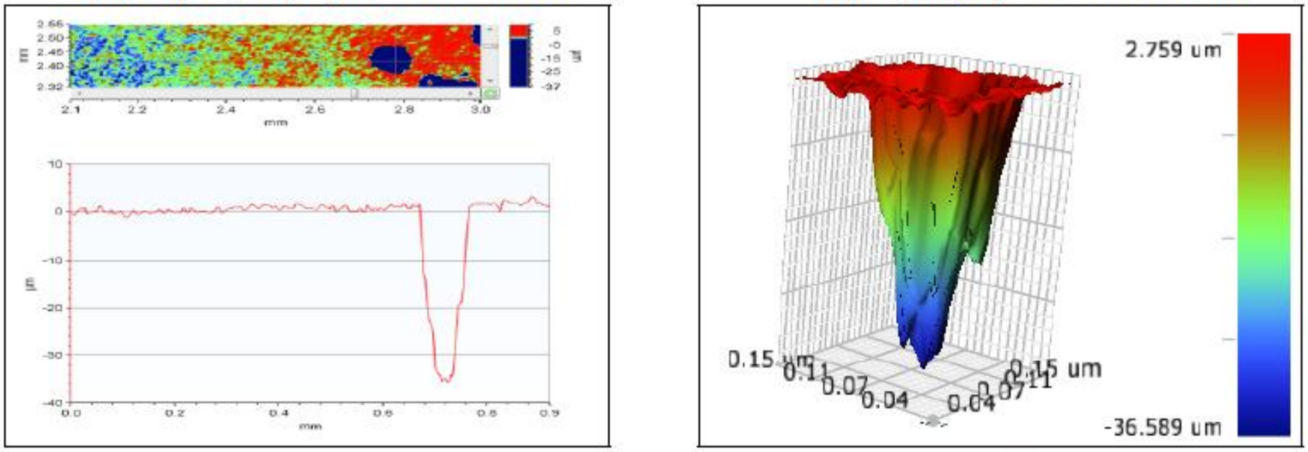

(c) **37** μ**m** pit (2D) for **3 mm Anode**

(d) **37** μ**m** pit (3D) for **3 mm Anode**

Figure 18: Morphology of maximum pit depth recorded on (a) 1 mm anode, (b) 2 mm anode and (c) 3 mm anode in artificial pit under saturated CO_2, 3.3 wt.% NaCl, 682 ppm Ca^{2+}, pH 7.5, 50 °C for 24 h

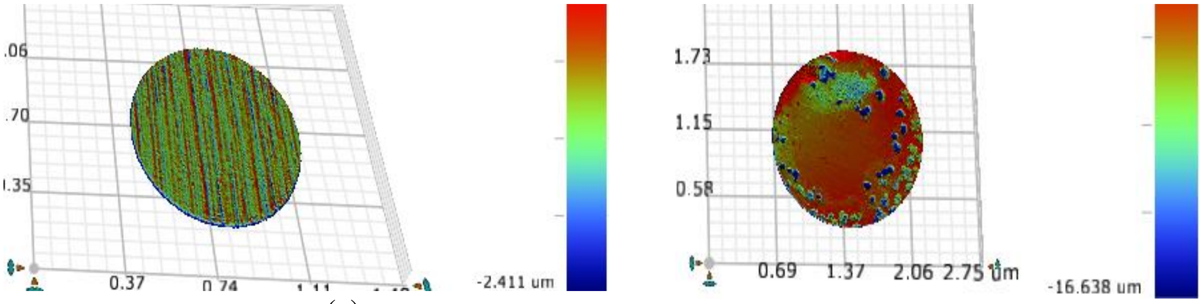

(a) (b)

Figure 19: Profilometry of 1mm anode (a) freshly polished before coupling into artificial pit assembly (b) after corrosion in an artificial pit

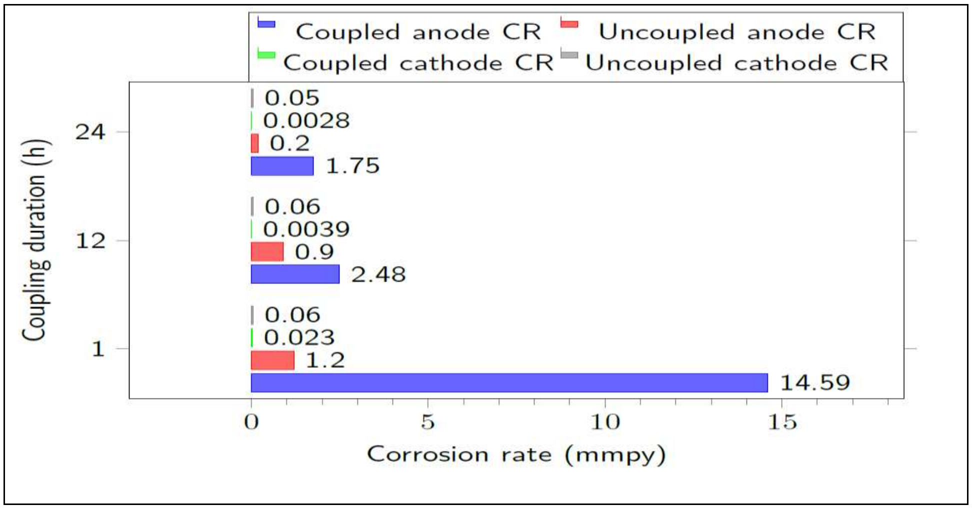

Figure 20: Chart depicting general corrosion rate (CR) for passivated cathode and freshly polished 1 mm anode electrode in coupled and uncoupled pit at experiment start, 12 h into test and towards test finishing under saturated CO_2, 3.3 wt.% NaCl, 682 ppm Ca^{2+}, pH 7.5, 50 °C

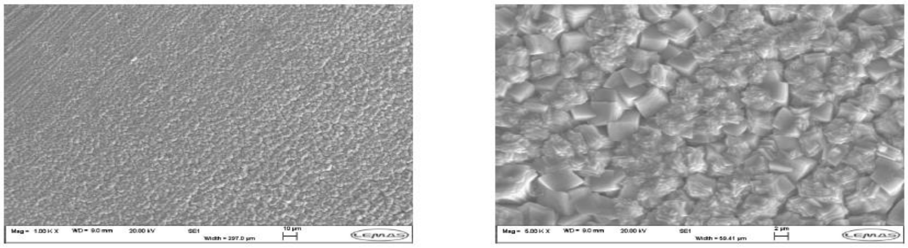

(a) X1000 (b) X5000

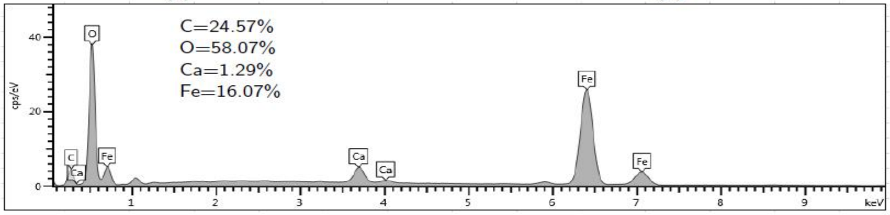

(c) Atomic composition

Figure 21: SEM results featuring (a) x1000 magnification (b) X5000 magnification and (c) atomic composition of mixed $CaCO_3$ and $FeCO_3$ formed on anode pin in 3.3 wt% NaCl, 682 ppm Ca^{2+}, pH 7.5, 50 °C for 24 h.

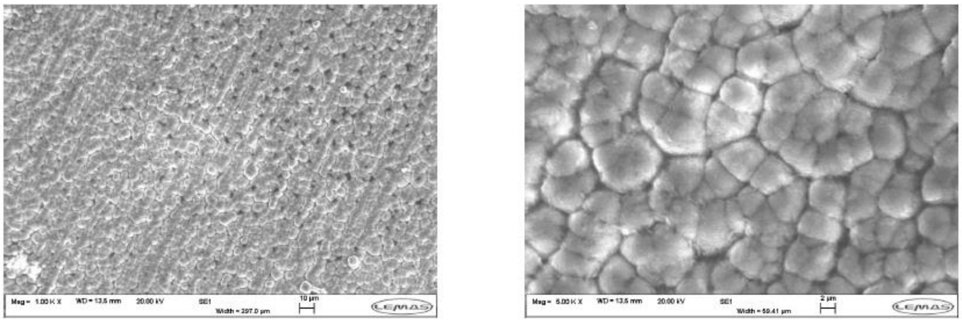

(a) X1000 (b) X5000

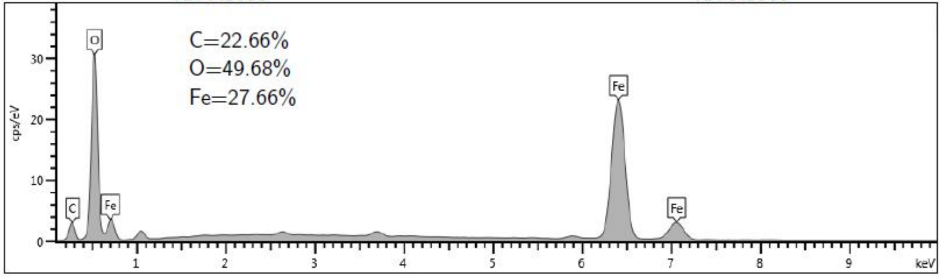

(c) Atomic composition

Figure 22: SEM results featuring (a) x1000 magnification (b) X5000 magnification and (c) atomic composition of $FeCO_3$ formed on anode pin in 3.5 wt% NaCl, 0 ppm Ca^{2+}, pH 7.5, 50 °C for 24 h

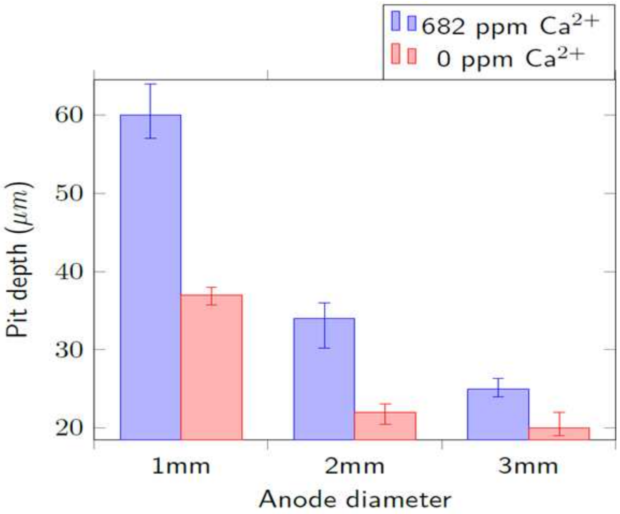

Figure 23: SEM results featuring (a) x1000 magnification (b) x5000 magnification and (c) atomic composition of $FeCO_3$ formed on anode pin in 3.5 wt% NaCl, 0 ppm Ca^{2+}, pH 7.5, 50 ◦C for 24 h

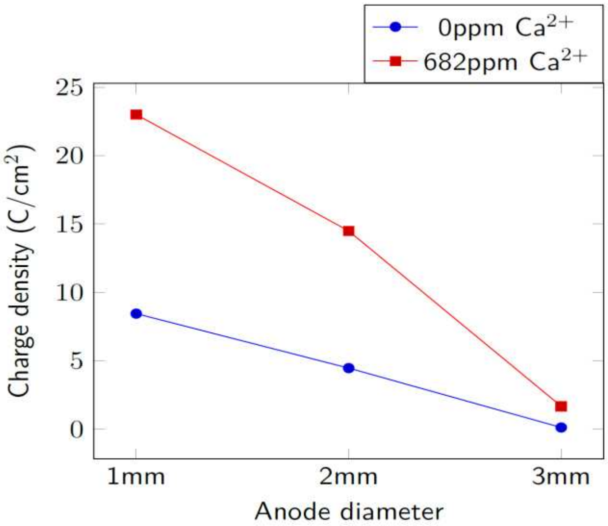

Figure 24: Plots depicting charge recorded for 1mm, 2mm and 3mm anode diameter in artificial pit coupling in saturated CO_2, 3.3 wt.% NaCl, pH 7.5, 50 ◦C in 682ppm Ca^{2+} and Ca^{2+}-free solutions.

Data Availability

The raw data required to reproduce the findings in this work are available to download upon request from ibejulekki@yahoo.co.uk or ibejulekki@icloud.com. Raw data were generated from the Institute of Functional Surfaces, University of Leeds, LS2 9JT. The processed data required to reproduce these findings are available to download upon request from the Corresponding author, Sikiru Adepoju Mohammed, Research and Development Centre, Defence Industries Corporation of Nigeria / Nigerian Defence Academy.

REFERENCES

[1] S. Mohammed, Y. Hua, R. Barker, and A. Neville, "Investigating pitting in X65 carbon steel using potentiostatic polarisation," ***Applied Surface Science,*** **vol. 423, pp. 25-32, 2017.**

[2] S. Zhang, L. Hou, H. Du, H. Wei, B. Liu, and Y. Wei, "Synergistic contribution of chloride and bicarbonate ions to pitting corrosion behavior of carbon steel," ***Corrosion,*** **vol. 75, pp. 1034-1043, 2019.**

[3] Z.-p. Zhao, K. Xu, P.-f. Xu, and B. Wang, "CO2 corrosion behavior of simulated heat-affected zones for X80 pipeline steel," ***Materials Characterization,*** **vol. 171, p. 110772, 2021.**

[4] J. Han, Y. Yang, S. Nesic, and B. N. Brown, "Roles of passivation and galvanic effects in localized CO2 corrosion of mild steel," in ***CORROSION 2008*****, 2008.**

[5] A. Dugstad, M. Seiersten, and R. Nyborg, "Flow assurance of pH stabilized wet gas pipelines," in ***CORROSION 2003*****, 2003.**

[6] S. Nešić, "Key issues related to modelling of internal corrosion of oil and gas pipelines–A review," ***Corrosion science,*** **vol. 49, pp. 4308-4338, 2007.**

[7] W. Li, B. Brown, D. Young, and S. Nešić, "Investigation of pseudo-passivation of mild steel in CO2 corrosion," ***Corrosion,*** **vol. 70, pp. 294-302, 2014.**

[8] J. Han, D. Young, H. Colijn, A. Tripathi, and S. Nešić, "Chemistry and structure of the passive film on mild steel in CO2 corrosion environments," ***Industrial & Engineering Chemistry Research,*** **vol. 48, pp. 6296-6302, 2009.**

[9] A. El-Sherik, ***Trends in oil and gas corrosion research and technologies: Production and transmission*****: Woodhead Publishing, 2017.**

[10] F. Pessu, R. Barker, and A. Neville, "The influence of pH on localized corrosion behavior of X65 carbon steel in CO2-saturated brines," ***Corrosion,*** **vol. 71, pp. 1452-1466, 2015.**

[11] X. Jiang, Y. Zheng, D. Qu, and W. Ke, "Effect of calcium ions on pitting corrosion and inhibition performance in CO2 corrosion of N80 steel," ***Corrosion science,*** **vol. 48, pp. 3091-3108, 2006.**

[12] A. M. Trevelin, R. E. Marotto, E. V. de Castro, G. P. Brandao, R. J. Cassella, and M. T. W. Carneiro, "Extraction induced by emulsion breaking for determination of Ba, Ca, Mg and Na in crude oil by inductively coupled plasma optical emission spectrometry," ***Microchemical Journal,*** **vol. 124, pp. 338-343, 2016.**

[13] R. B. Rebak and T. E. Perez, "Effect of carbon dioxide and hydrogen sulfide on the localized corrosion of carbon steels and corrosion resistant alloys," in ***CORROSION 2017*****, 2017.**

[14] A. M. Nejad and M. S. Karimi, "Investigation of the influence of scaling on corrosion behaviour of tubing in oil wells," *Int J Sci Technol Res,* vol. 6, pp. 109-113, 2017.

[15] S. Navabzadeh Esmaeely, Y.-S. Choi, D. Young, and S. Nešić, "Effect of calcium on the formation and protectiveness of iron carbonate layer in CO2 corrosion," *Corrosion,* vol. 69, pp. 912-920, 2013.

[16] G. Zhang and Y. Cheng, "Localized corrosion of carbon steel in a CO2-saturated oilfield formation water," *Electrochimica Acta,* vol. 56, pp. 1676-1685, 2011.

[17] J. Han, B. Brown, and S. Nešic, "Investigation of the galvanic mechanism for localized carbon dioxide corrosion propagation using the artificial pit technique," *Corrosion,* vol. 66, pp. 095003-095003-12, 2010.

[18] Y. Yang, B. Brown, and S. Nesic, "Electrochemical investigation of localized CO2 corrosion on mild steel," in *CORROSION 2007*, 2007.

[19] J. Han, S. Nešić, and B. N. Brown, "Galvanic Model for Localized CO2 Corrosion," *ICC/2008, paper,* 2008.

[20] R. M. Fernández-Domene, R. Leiva-García, J. Andrews, and R. Akid, "Galvanic corrosion following local breakdown of a scale formed on X-65 in CO2 saturated solutions," in *CORROSION 2015*, 2015.

[21] R. Newman, "The dissolution and passivation kinetics of stainless alloys containing molybdenum—II. Dissolution kinetics in artificial pits," *Corrosion science,* vol. 25, pp. 341-350, 1985.

[22] A. Turnbull, D. Coleman, and A. Griffiths, "Assessment of test methods for evaluating effectiveness of corrosion inhibitors in retarding propagation of localised corrosion," *British Corrosion Journal,* vol. 36, pp. 210-214, 2001.

[23] A. Turnbull, D. Coleman, A. Griffiths, P. Francis, and L. Orkney, "Effectiveness of corrosion inhibitors in retarding the rate of propagation of localized corrosion," *Corrosion,* vol. 59, 2003.

[24] J. Marsh, J. Palmer, and R. Newman, "Evaluation of inhibitor performance for protection against localized corrosion," *CORROSION/2002, paper,* vol. 2288, 2002.

[25] J. Amri, E. Gulbrandsen, and R. Nogueira, "Pit growth and stifling on carbon steel in CO2-containing media in the presence of HAc," *Electrochimica Acta,* vol. 54, pp. 7338-7344, 2009.

[26] S. Sisira, D. Alexander, K. Thomas, G. Vimal, K. P. Mani, P. Biju, N. Unnikrishnan, and C. Joseph, "Microstructural characterization and optical properties of green emitting hexagonal and monoclinic CePO4: Tb3+ nanocrystals," *Materials Research Express,* vol. 4, p. 025010, 2017.

[27] J. Singh, C. Singh, D. Kaur, S. B. Narang, R. Jotania, and R. Joshi, "Investigation on structural and microwave absorption property of Co2+ and Y3+ substituted M-type Ba-Sr hexagonal ferrites prepared by a ceramic method," *Journal of Alloys and Compounds,* vol. 695, pp. 792-798, 2017.

[28] S. N. Esmaeely, D. Young, B. Brown, and S. Nešić, "Effect of incorporation of calcium into iron carbonate protective layers in CO2 corrosion of mild steel," *Corrosion,* vol. 73, pp. 238-246, 2017.

[29] P. M. Davidson, G. H. Symmes, B. A. Cohen, R. J. Reeder, and D. H. Lindsley, "Synthesis of the new compound CaFe (CO3) 2 and experimental constraints on the (Ca, Fe) CO3 join," *Geochimica et Cosmochimica Acta,* vol. 57, pp. 5105-5109, 1993.

[30] Y. Wang, J. Wang, and X. Zhang, "The electrochemical corrosion properties of PANI/coal composites on magnesium alloys," *Int. J. Electrochem. Sci,* vol. 12, pp. 4044-4055, 2017.